

Article

Thermodynamic Properties of Stoichiometric Non-Superconducting Phase Y_2BaCuO_5

Filip Antončík¹, David Sedmidubský^{1,*} , Adéla Jiříčková¹, Michal Lojka¹, Tomáš Hlášek², Květoslav Růžička³ and Ondřej Jankovský¹

¹ Department of Inorganic Chemistry, Faculty of Chemical Technology, University of Chemistry and Technology, Technická 5, 166 28 Prague, Czech Republic; Filip.Antoncik@vscht.cz (F.A.); Adela.Jirickova@vscht.cz (A.J.); michal.lojka@vscht.cz (M.L.); ondrej.jankovsky@vscht.cz (O.J.)

² Can Superconductors, 251 68 Kamenice, Czech Republic; tomas.hlasek@cansuperconductors.com

³ Department of Physical Chemistry, Faculty of Chemical Technology, University of Chemistry and Technology, Technická 5, 166 28 Prague, Czech Republic; ruzickak@vscht.cz

* Correspondence: sedmidub@vscht.cz; Tel.: +420-220-44-4122

Received: 21 August 2019; Accepted: 25 September 2019; Published: 27 September 2019



Abstract: Y_2BaCuO_5 often occurs as an accompanying phase of the well-known high-temperature superconductor $YBa_2Cu_3O_7$ (also known as YBCO). Y_2BaCuO_5 , easily identifiable due to its characteristic green coloration, is often referred to as ‘green phase’ or ‘Y-211’. In this contribution, Y_2BaCuO_5 phase was studied in detail with a focus on its thermal and thermodynamic properties. Energy dispersive spectroscopy (EDS), X-ray diffraction (XRD), and scanning electron microscopy (SEM) were employed in the study of sample’s morphology and chemical composition. XRD data were further analyzed and lattice parameters refined by Rietveld analysis. Simultaneous thermal analysis was employed to study thermal stability. Particle size distribution was analyzed by laser diffraction. Finally, thermodynamic properties, namely heat capacity and relative enthalpy, were measured by drop calorimetry, differential scanning calorimetry (DSC), and physical properties measurement system (PPMS). Enthalpy of formation was assessed from ab-initio DFT calculations.

Keywords: Y-211; superconductors; Y_2BaCuO_5 ; thermodynamic properties; YBCO

1. Introduction

Transition metal (TM) oxides constitute a large family of oxides, which possess a variety of interesting properties [1–4]. Cobalt mixed oxides with misfit structure are thermoelectric materials for the recovery of waste heat, and misfit cobaltites also show unique catalytic properties [5–7]. Mixed oxides containing lithium found a crucial application in accumulator industry [8]. Nano-sized oxides are widely used in catalysis, electrochemistry, and solar cells [9–13]. Among TM oxides, the high-temperature superconductors (HTS) revealing critical temperature close to the temperature of liquid nitrogen have been attracting permanent attention since their discovery in 1986 [14]. Although enhanced critical temperatures and intriguing superconducting behavior have been later reported in several systems, for example in layered ternary and quaternary arsenide systems [15,16], the HTS cuprates became the most wide-spread group of high-temperature superconductors, still being at the forefront of both theoretical and applied research in the field of superconductivity.

Their discovery in the Ba–La–Cu–O system [14] was immediately followed by an intensive search for novel HTS phases in congeners systems such as Y–Ba–Cu–O, Bi–Sr–Ca–Cu–O, Tl–Ba–Ca–Cu–O, and Hg–Ba–Ca–Cu–O [17–25]. Superconducting phases in these systems are usually derived from perovskites by inserting other structural motifs such as rock-salt type blocks, and thus forming layered structures. In general, perovskites and similar layered oxides exhibit a wide variety of

interesting properties, such as high electrochemical stability, catalytic activity, low electric resistivity, and low thermal conductivity [26–29]. For the properties listed above, layered inorganic oxides are still studied extensively, even to this day. One of the most significant systems relevant to HTS is the quasi-ternary Y–Ba–Cu–O system [30], with $\text{YBa}_2\text{Cu}_3\text{O}_{7-\delta}$ (YBCO) being the superconductive phase [31]. This phase is usually accompanied by Y_2BaCuO_5 [32–35], which is often formed during the solid-state reaction [36], as a result of surplus of yttrium. This can be caused by partial melting during the processing yielding a Ba- and Cu-rich melt, which subsequently crystallizes into $\text{Ba}_3\text{Cu}_5\text{O}_8$ phase during cooling if the equilibrium is not achieved. As a result, the rest of the system is shifted towards Y-rich compositions, inducing a formation of Y_2BaCuO_5 . However, this effect is not necessarily detrimental for the superconductivity of the material, since Y_2BaCuO_5 , if properly nanostructured, can act as a source of pinning centers for vortices. The goal of this paper is to study Y_2BaCuO_5 phase that is present in single-domain YBCO superconductors in a form of pinning centers. The main focus is put on the thermal properties, which are decisive for tailoring the material properties by high temperature processing.

Similarly to $\text{YBa}_2\text{Cu}_3\text{O}_{7-\delta}$, copper is five-fold coordinated by oxygen atoms; however, the tetragonal pyramids are not interconnected, yielding an insulating ground state. Moreover, at temperatures below 30 K, an antiferromagnetic arrangement of spins $\frac{1}{2}$ localized on Cu(+II) sites is established [37]. These physical characteristics have to be considered when interpreting the heat capacity at low temperatures.

In our contribution, we prepared pure polycrystalline phase Y_2BaCuO_5 . Phase purity, morphology, and thermal and thermodynamic properties were studied in detail. The precise knowledge of thermodynamic properties of phases involved in the Y–Ba–Cu–O system is essential for modeling phase equilibria in YBCO-based superconducting materials (including systems with additional components) and tailoring their micro/nanostructural characteristics to enhance their performance.

2. Materials and Methods

We used the following chemicals for the synthesis of Y_2BaCuO_5 : Barium carbonate (Sigma-Aldrich, Prague, Czech Republic; 99 + %), yttrium (III) oxide (Chemapol, Prague, Czech Republic; 99.99%), and copper (II) oxide (Sigma-Aldrich; 99.99%). Powders were homogenized in the ratio corresponding to Y_2BaCuO_x stoichiometry and repeatedly calcined in corundum crucible at 1123 K for 12 h, then at temperatures of 1138 K, 1153 K, and 1163 K for 24 h with a homogenization between each step. Finally, the sample was pressed into pellets and calcined for additional 24 h at 1173 K. The sample was slowly cooled in order to obtain a thermodynamically stable phase fully saturated with oxygen. The sample with the stoichiometry Y_2BaCuO_5 is termed Y-211 hereinafter.

X-ray powder diffraction (XRD) was measured at 298 K on Bruker D8 Discoverer powder diffractometer (Bruker, Karlsruhe, Germany) in a standard parafocusing Bragg–Brentano geometry using CuK_α radiation ($\lambda = 1.5418 \text{ \AA}$, $U = 40 \text{ kV}$, $I = 40 \text{ mA}$). Rietveld refinement fit was performed using Topas software v. 5 (Bruker, Karlsruhe, Germany).

The microstructure was analyzed using scanning electron microscopy (SEM). The elemental composition was studied using energy-dispersive spectroscopy (EDS) analyzer X-Max^N with 20 mm² silicon drift detector from Oxford instruments (Abingdon, UK) and software package Aztec Energy v. 3 (Asylum Research-Nanoanalysis, Wycombe, UK) using a Tescan Lyra dual beam microscope (Tescan, Brno, Czech Republic) with a field emission gun electron source.

The thermal stability Y_2BaCuO_5 was analyzed by simultaneous thermal analysis (STA) using Setaram Setsys Evolution (Setaram, Lyon, France). The heating rate during the measurement performed in dynamic air atmosphere ($50 \text{ cm}^3 \text{ min}^{-1}$) was 10 K min^{-1} .

The particle size distribution was analyzed by the laser diffraction method; Malvern Panalytical Mastersizer 3000 device (Malvern, UK) with 4 mW He–Ne 632.8 nm Red light source and 10 mW LED 470 nm Blue light source was used. The range of measurement was set from 0.1 to 1000 μm . The measurement was done using dispersion (1 g/100 mL) of the material in isopropyl alcohol. Y-211 sample was measured 5 times (5 scans) and distribution was created as an average value.

The heat capacity in the low-temperature region was measured using the physical properties measurement system (PPMS) equipment, Evercool-II 9 T-type (Quantum Design, San Diego, CA, USA). The heat capacity was obtained by the relaxation method under high vacuum.

A Tian–Calvet-type calorimeter μ DSC IIIa (Setaram, Lyon, France) was used for the measurement of heat capacities in the temperature range 262 to 358 K, employing NIST Standard reference material No. 720 as a reference material. Performance of the calorimeter is regularly checked by measurement of compounds with well-established C_{pm} data (naphthalene, benzophenone, benzoic acid). Based on these checking experiments, the combined expanded uncertainty of the heat capacity measurements is estimated to be $U_c(C_{pm}) = 0.01 C_{pm}$. More details can be found in paper [38]. Data obtained from this calorimeter are referred as DSC data.

Multi HTC 96 (Setaram, Lyon, France) high-temperature calorimeter (operated in a static air atmosphere) was used to measure enthalpy increments. The measurement was performed by dropping of the reference material (synthetic sapphire, NIST No. 720) and the sample in the sequence standard–sample–standard–sample–standard. The delays between two subsequent drops were 25 min in order to stabilize the heat flow. The estimated combined expanded uncertainty of the heat capacity measurements is estimated to be $U_c(C_{pm}) = 0.03 C_{pm}$.

Enthalpy of formation was assessed from ab-initio density functional theory (DFT)-based calculations. The electronic structure and total energies of Y_2BaCuO_5 and the constituent oxides, Y_2O_3 , BaO, and CuO, were calculated by means MedeA-VASP [39] program using projector augmented plane waves basis set and generalized gradient approximation (GGA-PBE0 [40]) to exchange-correlation functional combined with additional local orbital specific coulomb potential $U = 3$ eV acting on Cu-3d states [41]. An antiferromagnetic ground state was considered for both CuO [42] and Y_2BaCuO_5 [37]. The basis set with a cut-off energy of 400 eV was applied. The k-point mesh was constructed inside the first Brillouin zone with k-point spacing smaller than 0.25 \AA^{-1} . A tetrahedron integration scheme was applied for electron density of states calculation.

3. Results and Discussion

Figure 1 shows the XRD pattern of the prepared Y_2BaCuO_5 sample. No visible impurities were detected by X-ray diffraction, only the presence of the Y-211 phase (Y_2BaCuO_5). The Rietveld fit (based on the orthorhombic space group $Pnma$) was applied to refine the lattice parameters. The following lattice parameters were obtained: $a = 12.134 \text{ \AA}$, $b = 5.6614 \text{ \AA}$, and $c = 7.1347 \text{ \AA}$ ($\alpha = \beta = \gamma = 90^\circ$ being fixed). The obtained data are in good agreement with the already published results $a = 12.1630 \text{ \AA}$, $b = 5.6490 \text{ \AA}$, and $c = 7.1230 \text{ \AA}$ (JCPDS 01-078-2214).

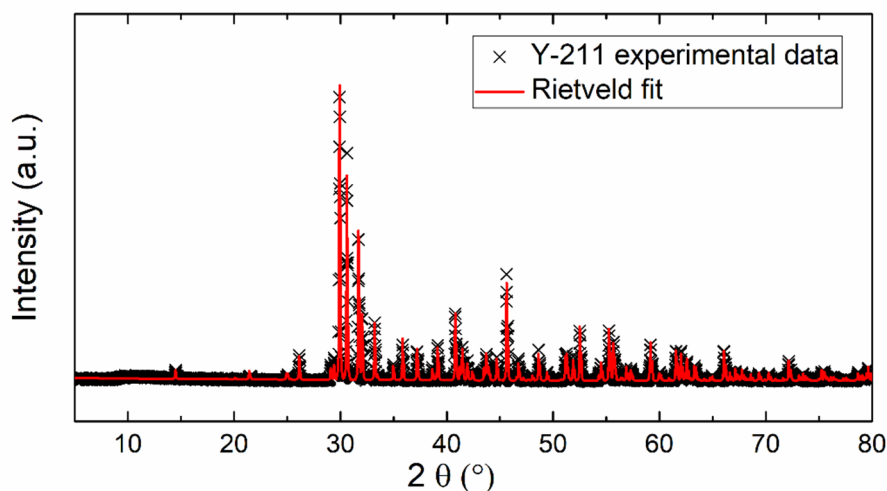


Figure 1. XRD powder diffractogram and Rietveld fit of experimental data.

SEM micrographs of the sample show that the Y_2BaCuO_5 particle size lies mostly between 1 and 5 μm ; the particle size remained very homogeneous across the sample, as can be seen from Figure 2a. This is in good agreement with the microstructures typically observed in polycrystalline cuprates. Elemental distribution maps were obtained by EDS and can be seen in Figure 2b. The sample appears to be homogenous and pure from a chemical point of view. Only Y, Ba, Cu, and O were detected. These results correspond with the results obtained by X-ray diffraction and confirm purity and phase composition of the prepared sample.

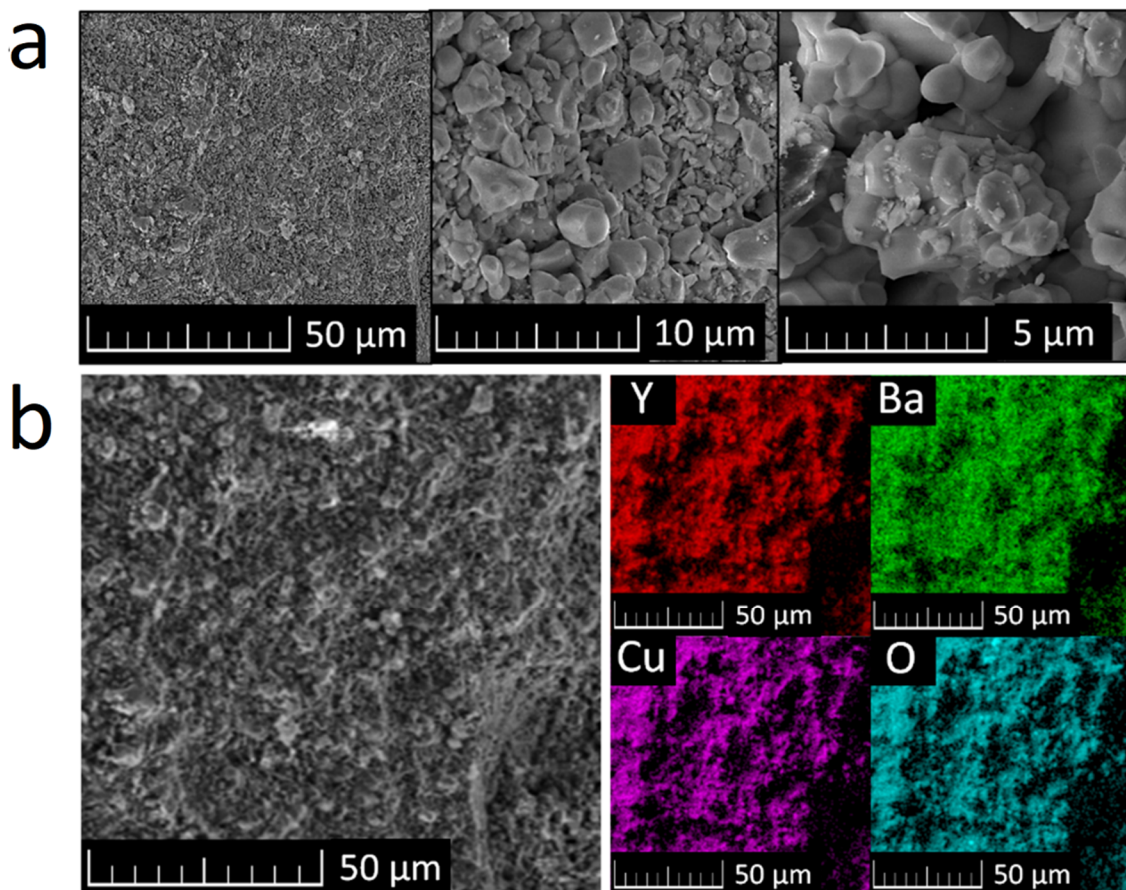


Figure 2. Y_2BaCuO_5 SEM micrographs (a) and elemental distribution maps of obtained by EDS (b).

In order to confirm the sizes of grains obtained from SEM, the powder was also analyzed by laser diffraction. Particle size distribution is shown in Figure 3, revealing that the grains are mainly of the size between 1 and 10 μm , $d_x(50) = 5.2 \mu\text{m}$, $d_x(10) = 2.8 \mu\text{m}$ and $d_x(90) = 10.3 \mu\text{m}$. These data are in good agreement with SEM.

Simultaneous thermal analysis (STA) was employed to study the thermal behavior of Y_2BaCuO_5 (Figure 4). The phase Y-211 decomposed in air atmosphere at 1551 K. Throughout the measurement, the mass was almost constant, i.e., the phase was stable up to temperatures of $\sim 1550 \text{ K}$ and we did not detect any release of oxygen, suggesting the presence of the stoichiometric phase. The weight decrease related to the original mass of Y_2BaCuO_5 was approximately 1 wt % suggesting formation of Y_2O_3 (s), BaO (s), and Cu-O (l).

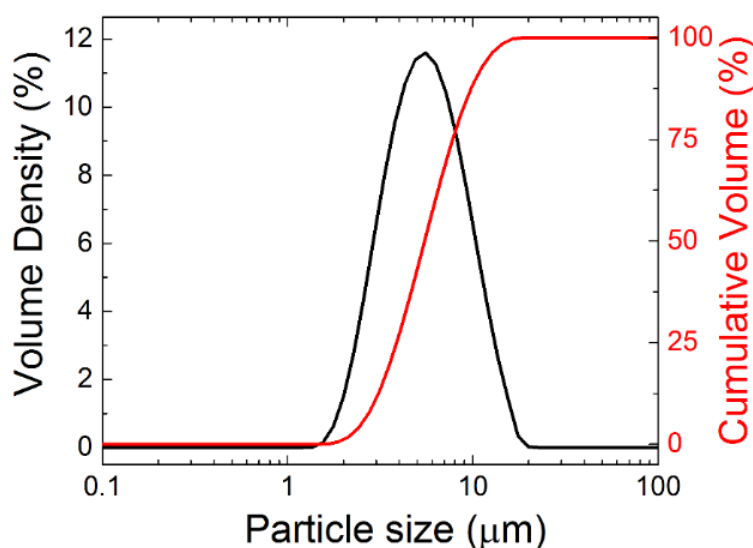


Figure 3. Particle size distribution of Y_2BaCuO_5 powder using laser diffraction.

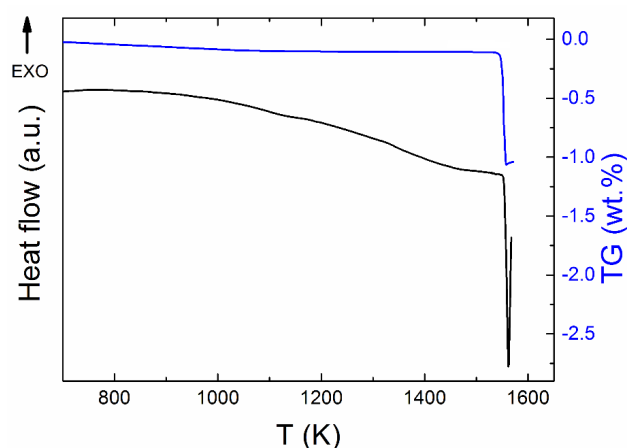


Figure 4. STA measurement of Y_2BaCuO_5 in dynamic air atmosphere.

The measured calorimetric data used for further analysis involved 37 C_{pm} values from relaxation time method (30–257 K), 40 C_{pm} values from DSC (263–354 K) (see Figures 5 and 6), and 16 values of the enthalpy increments from the drop measurements from the range 573–1273 K (see Figure 7).

For further analysis of low temperature heat capacity data, two sets of the C_{pm} data (relaxation time + DSC) were considered. Since the studied material is a magnetic insulator, only the lattice part of heat capacity is relevant for temperatures well above the Néel temperature, $T = 16.2$ K. For this reason, only the data above 30 K were considered for the analysis of phonon heat capacity, which was performed using the combination of the Debye and Einstein models according to the following Equation (1):

$$C_{phD} = R \left[9 \left(\frac{T}{\Theta_D} \right)^3 \int_0^{x_D} \frac{x_D^4 \exp(x_D)}{(\exp(x_D) - 1)^2} dx + \sum_{i=1}^3 \frac{w_i x_{Ei}^2 \exp(x_{Ei})}{(\exp(x_{Ei}) - 1)^2} \right] \quad (1)$$

Here R is the gas constant, θ_D and θ_{Ei} are the Debye and Einstein characteristic temperatures, and $x_D = \theta_D/T$, $x_{Ei} = \theta_{Ei}/T$, and w_i refer to a degeneracy of the corresponding Einstein mode.

It is a well-known fact that the phonon spectrum of a mixed oxide contains $3n-3$ optical branches and three acoustic branches (n is number of atoms per formula unit). In Y_2BaCuO_5 , there are 9 atoms per formula unit representing 24 optical branches which were grouped into three 8-fold degenerate Einstein modes.

The Debye–Einstein model is based on a harmonic crystal approximation describing the heat capacity at constant volume. As can be seen Figure 6, the experimentally obtained heat capacity exceeded the Dulong–Petit limit valid for C_V at ~ 670 K. It was previously described [43] that a multiplication factor $1/(1-\alpha T)$ can be introduced to any vibration mode (in order to take into account the anharmonic effects) and to describe the C_p-C_V difference using a semi-empirical approach. Hence, in our analysis, we used such an anharmonicity parameter that was combined only with the Debye mode in Equation (1). The analysis of the phonon heat capacity is shown in Table 1. The fitted curve based on PPMS and DSC data corresponding to LT-fit in Figure 5 describes the low temperature data satisfactorily above 60 K. Below this temperature, a substantial excess term due to magnetic ordering is clearly visible (see the inset in Figure 5).

Table 1. Evaluated parameters of Debye–Einstein model based on PPMS and DSC data.

Mode (<i>i</i>)	<i>D</i>	<i>E</i> ₁	<i>E</i> ₂	<i>E</i> ₃	<i>D</i>
<i>w_i</i>	3	8	8	8	-
<i>θ_i/K</i>	116.3 ± 1.7	263.6 ± 2.0	406.7 ± 3.0	774.0 ± 3.9	(6.584 ± 0.120) × 10 ⁻⁴

The absolute entropy at the reference temperature ($T = 298.15$ K) was obtained by integrating the experimental data of the heat capacity divided by the thermodynamic temperature from 2 K up to ambient temperature as $S_m(298.15) = 209.47$ J mol⁻¹ K⁻¹. This experimental value can be decomposed into a lattice vibrations contribution, $S_{lat}(298.15) = 206.9$ J mol⁻¹ K⁻¹, and an excess entropy due to magnetic ordering disruption $S_{lat}(298.15) = 2.8$ J mol⁻¹ K⁻¹, which is about two times lower than the theoretical value $R \ln 2$ corresponding to spin $\frac{1}{2}$ of Cu(+II) and also lower than the experimental value reported by Knafo et al. [43] who, however, derived the phonon contribution by scaling the C_p data of YBa₂Cu₃O₇.

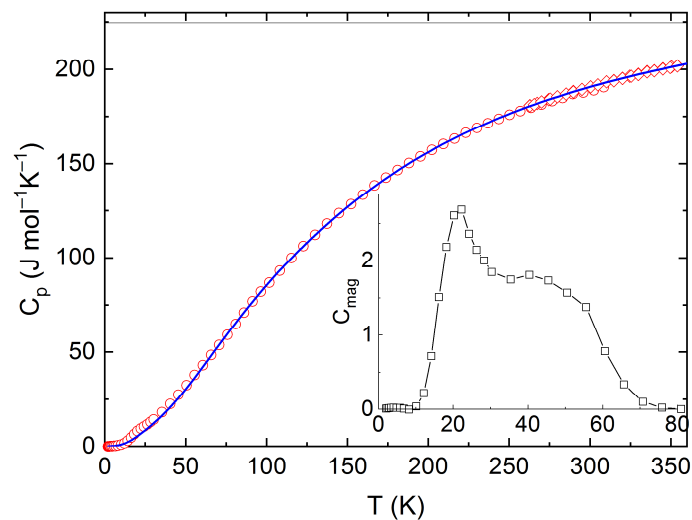


Figure 5. Low temperature heat capacity of Y₂BaCuO₅ obtained from PPMS and DSC, including the Debye–Einstein fit and the excess magnetic term in the inset.

Above room temperature, dependence of the heat capacity was also determined. The linear least-squares method was used for treatment of the heat capacity data from DSC and the enthalpy increment data from drop calorimetry. The temperature dependence of C_{pm} was obtained in Equation (2):

$$C_{pm} = A + B \times T + C \times T^{-2} \quad (2)$$

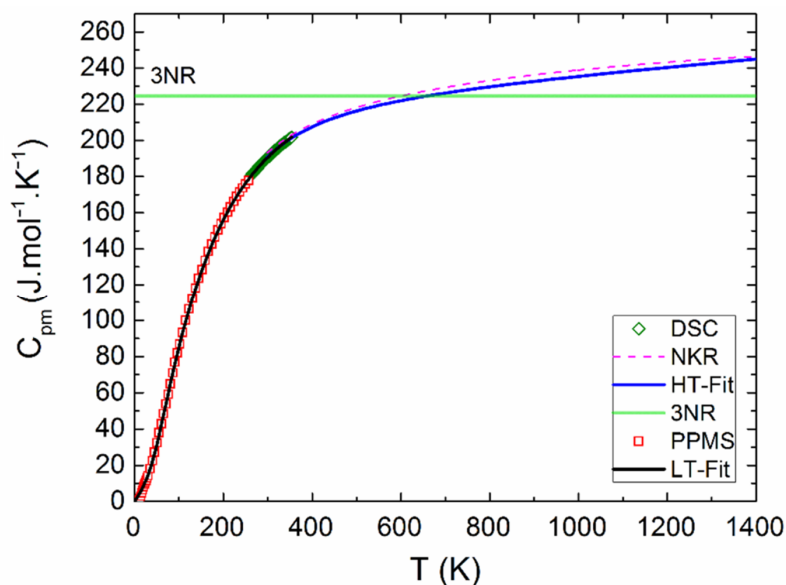


Figure 6. Heat capacity of Y_2BaCuO_5 obtained from PPMS and HT-fit.

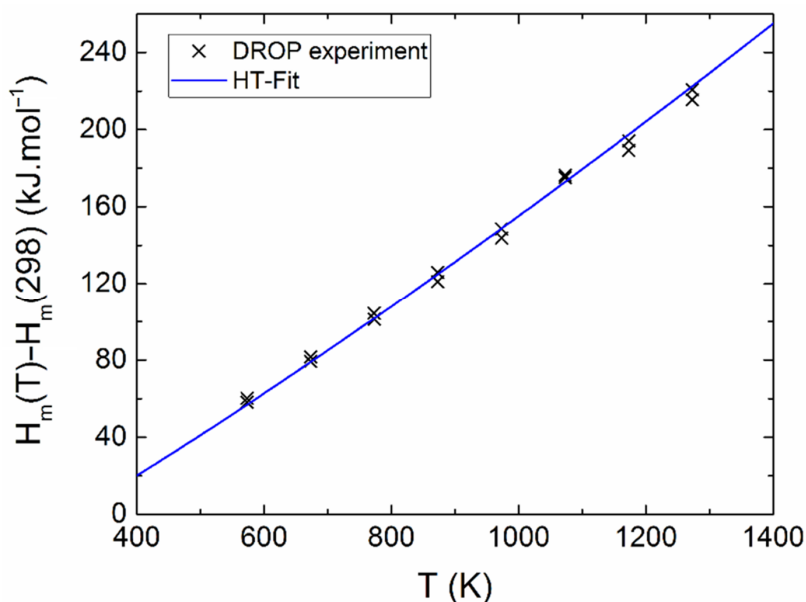


Figure 7. Relative enthalpy of Y_2BaCuO_5 obtained from drop experiments.

Let us note that the related temperature function of enthalpy, $\Delta H_m(T) = H_m(T) - H_m(T_0)$, is given by the following Equation (3):

$$\Delta H(T) = H(T) - H(T_0) = A \times (T - T_0) + \frac{1}{2}B \times (T^2 - T_0^2) - C \times \left(\frac{1}{T} - \frac{1}{T_0} \right) \quad (3)$$

The sum of squares was applied on both functions, Equations (2) and (3), and both sets of data were simultaneously minimized. Different weights w_i were assigned to the individual points (calculated as $w_i = 1/\delta_i$, where δ_i is the absolute error bar). The obtained temperature dependence of heat capacity can be expressed as (valid between 298 and 1400 K) Equation (4):

$$C_{pm} = (201.776 \pm 10.531) + (0.041175 \pm 0.016247) \times T - (2.21863 \pm 0.3590) \times 10^6 \times T^{-2} \quad (4)$$

We compared obtained data with the curve calculated using the Neumann–Kopp rule (NKR), where the heat capacity of Y_2BaCuO_5 was evaluated by the following Equation (5):

$$C_{pm}(\text{Y}_2\text{BaCuO}_5) = C_{pm}(\text{Y}_2\text{O}_3) + C_{pm}(\text{BaO}) + C_{pm}(\text{CuO}) \quad (5)$$

As can be seen from Figure 6, our data are in good agreement with the calculated NKR curve, suggesting that the lattice dynamics—including the anharmonic effects—are comparable in Y_2BaCuO_5 and the constituent binary oxides.

We took advantage of this similarity in chemical bonding and used the binary oxides as a reference for evaluating the enthalpy of formation from GGA+U ab-initio calculations. Hence, the ground state enthalpy of formation from oxides, $\Delta_{\text{ox}}H = -32.2 \text{ kJ mol}^{-1}$, is the primary value derived from DFT while the enthalpy of formation from elements, $\Delta_f H = -2640.9 \text{ kJ mol}^{-1}$, was obtained from $\Delta_{\text{ox}}H$ and the tabulated $\Delta_f H$ values of the binary oxides. The enthalpy of formation is underestimated compared to dissolution calorimetry results $\Delta_f H = -2656 \text{ kJ mol}^{-1}$ [44] and $-2660 \text{ kJ mol}^{-1}$ [45]. A part of this discrepancy can be accounted for by the negative integral of $\Delta_{\text{ox}}C_p$ used to recalculate the ab-initio value from 0 to 298 K, for which the experimental data are reported.

Let us note that the magnetic structure has a substantial effect on the resulting value of $\Delta_{\text{ox}}H$. Here, we present the results for A-type spin arrangement (two spins $+\frac{1}{2}$ and two spins $-\frac{1}{2}$ within the chemical unit cell) and no magnetic superstructure. The resulting density of states for both spin channels is shown in Figure 8. The spin polarization on copper sites clearly visible on Cu(1)-3d projection in Figure 8 amounts to 0.59 Bohr magnetons, which is in nice agreement with the neutron diffraction data ($0.55 \mu\text{B}$) [37]. If we considered the F type arrangement (all four spins aligned parallel) in the chemical unit cell and a magnetic superstructure with the wave vector $k = [0, \frac{1}{2}, \frac{1}{2}]$, which has been reported as an alternative ordering, the calculation converged to a non-spin polarized state and $\Delta_{\text{ox}}H = -0.5 \text{ kJ mol}^{-1}$. Interestingly, a similar result (zero spin and low stabilization) was obtained for A-type ordering and $k = [0, \frac{1}{2}, \frac{1}{2}]$ superstructure. Hence, the magnetic superstructure reported in [37] was not confirmed.

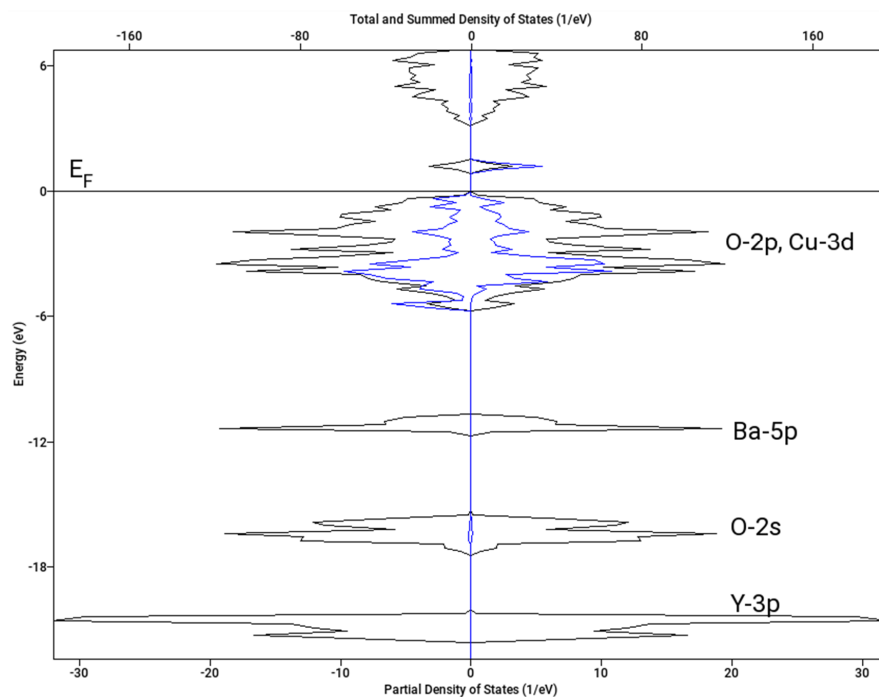


Figure 8. Calculated density of states (DOS) of Y_2BaCuO_5 (A-type antiferromagnetic arrangement). Spin-down projections is shown as negative. Total DOS—black line; Cu-3d projection for Cu(1) atom with down majority spin—blue line. Fermi level (E_F) is set to 0 eV.

4. Conclusions

In our contribution, we prepared a polycrystalline cuprate Y_2BaCuO_5 by conventional solid-state reaction. The sample was thoroughly analyzed in order to ensure its purity. Morphology and thermal properties were further studied in detail. Using X-ray diffraction, we confirmed the presence of pure Y_2BaCuO_5 without any detectable impurities. Very high thermal stability (up to ~ 1550 K) of Y_2BaCuO_5 (compared to phase $YBa_2Cu_3O_7$) is important for its inert behavior during the manufacturing of YBCO bulk ceramics. Moreover, the obtained calorimetry data are important for thermodynamic modeling of high temperature material processing, which can underpin future development of high-temperature superconductors and their possible applications in superconducting bearings, transport, or superconducting transmission lines.

Author Contributions: Conceptualization, O.J. and D.S.; investigation, F.A., M.L., A.J., K.R. and T.H.; writing—original draft preparation, F.A.; writing—review and editing, O.J. and D.S.

Funding: This research was funded by the Czech Science Foundation, grant number 17-13161S. This research was also funded by TACR, program THETA, grant number TK01030200.

Conflicts of Interest: The authors declare no conflict of interest.

References

1. Yuan, C.; Wu, H.B.; Xie, Y.; Lou, X.W. Mixed transition-metal oxides: Design, synthesis, and energy-related applications. *Angew. Chem. Int. Ed.* **2014**, *53*, 1488–1504. [[CrossRef](#)]
2. Zhao, Y.; Li, X.; Yan, B.; Xiong, D.; Li, D.; Lawes, S.; Sun, X. Recent developments and understanding of novel mixed transition-metal oxides as anodes in lithium ion batteries. *Adv. Energy Mater.* **2016**, *6*, 1502175. [[CrossRef](#)]
3. Jankovský, O.; Sedmidubský, D.; Šimek, P.; Sofer, Z.; Ulbrich, P.; Bartůněk, V. Synthesis of MnO , Mn_2O_3 and Mn_3O_4 nanocrystal clusters by thermal decomposition of manganese glycerolate. *Ceram. Int.* **2015**, *41*, 595–601. [[CrossRef](#)]
4. Bartůněk, V.; Huber, Š.; Sedmidubský, D.; Sofer, Z.; Šimek, P.; Jankovský, O. CoO and Co_3O_4 nanoparticles with a tunable particle size. *Ceram. Int.* **2014**, *40*, 12591–12595. [[CrossRef](#)]
5. Kang, M.-G.; Cho, K.-H.; Kim, J.-S.; Nahm, S.; Yoon, S.-J.; Kang, C.-Y. Post-calcination, a novel method to synthesize cobalt oxide-based thermoelectric materials. *Acta Mater.* **2014**, *73*, 251–258. [[CrossRef](#)]
6. Prasad, K.R.; Miura, N. Electrochemically synthesized MnO_2 -based mixed oxides for high performance redox supercapacitors. *Electrochem. Commun.* **2004**, *6*, 1004–1008. [[CrossRef](#)]
7. Rao, K.; Smakula, A. Dielectric properties of cobalt oxide, nickel oxide, and their mixed crystals. *J. Appl. Phys.* **1965**, *36*, 2031–2038. [[CrossRef](#)]
8. Van Schalkwijk, W.; Scrosati, B. Advances in lithium ion batteries introduction. In *Advances in Lithium-Ion Batteries*; Kluwer Academic/Plenum Publisher: London, UK, 2002; pp. 1–5.
9. Andersen, N.I.; Serov, A.; Atanassov, P. Metal oxides/CNT nano-composite catalysts for oxygen reduction/oxygen evolution in alkaline media. *Appl. Catal. B Environ.* **2015**, *163*, 623–627. [[CrossRef](#)]
10. Jayalakshmi, M.; Rao, M.M.; Venugopal, N.; Kim, K.-B. Hydrothermal synthesis of SnO_2 - V_2O_5 mixed oxide and electrochemical screening of carbon nano-tubes (CNT), V_2O_5 , V_2O_5 -CNT, and SnO_2 - V_2O_5 -CNT electrodes for supercapacitor applications. *J. Power Sour.* **2007**, *166*, 578–583. [[CrossRef](#)]
11. Ito, S.; Makari, Y.; Kitamura, T.; Wada, Y.; Yanagida, S. Fabrication and characterization of mesoporous SnO_2 /ZnO-composite electrodes for efficient dye solar cells. *J. Mater. Chem.* **2004**, *14*, 385–390. [[CrossRef](#)]
12. Rusevova, K.; Kopinke, F.-D.; Georgi, A. Nano-sized magnetic iron oxides as catalysts for heterogeneous Fenton-like reactions—Influence of Fe (II)/Fe (III) ratio on catalytic performance. *J. Hazard. Mater.* **2012**, *241*, 433–440. [[CrossRef](#)]
13. Leitner, J.; Bartůněk, V.; Sedmidubský, D.; Jankovský, O. Thermodynamic properties of nanostructured ZnO. *Appl. Mater. Today* **2018**, *10*, 1–11. [[CrossRef](#)]
14. Bednorz, J.G.; Müller, K.A. Possible high T_c superconductivity in the Ba–La–Cu–O system. *Z. Phys. B Condens. Matter* **1986**, *64*, 189–193. [[CrossRef](#)]

15. Rotter, M.; Tegel, M.; Johrendt, D. Superconductivity at 38 K in the iron arsenide $(\text{Ba}_{1-x}\text{K}_x)\text{Fe}_2\text{As}_2$. *Phys. Rev. Lett.* **2008**, *101*, 107006. [[CrossRef](#)]
16. Tallapally, V.; Damma, D.; Darmakkolla, S.R. Facile synthesis of size-tunable tin arsenide nanocrystals. *Chem. Commun.* **2019**, *55*, 1560–1563. [[CrossRef](#)]
17. Sleight, A.W.; Gillson, J.; Bierstedt, P. High-temperature superconductivity in the $\text{BaPb}_{1-x}\text{Bi}_x\text{O}_3$ system. *Solid State Commun.* **1993**, *88*, 841–842. [[CrossRef](#)]
18. Paglione, J.; Greene, R.L. High-temperature superconductivity in iron-based materials. *Nat. Phys.* **2010**, *6*, 645. [[CrossRef](#)]
19. Jankovský, O.; Antončík, F.; Hlášek, T.; Plecháček, V.; Sedmidubský, D.; Huber, Š.; Lojka, M.; Bartůněk, V. Synthesis and properties of $\text{YBa}_2\text{Cu}_3\text{O}_{7-\delta}$ - $\text{Y}_2\text{Ba}_4\text{CuWO}_{10}$ superconducting composites. *J. Eur. Ceram. Soc.* **2018**, *38*, 2541–2546. [[CrossRef](#)]
20. Drozdov, A.; Eremets, M.; Troyan, I.; Ksenofontov, V.; Shylin, S. Conventional superconductivity at 203 kelvin at high pressures in the sulfur hydride system. *Nature* **2015**, *525*, 73. [[CrossRef](#)]
21. Wang, X.; Liu, Q.; Lv, Y.; Gao, W.; Yang, L.; Yu, R.; Li, F.; Jin, C. The superconductivity at 18 K in LiFeAs system. *Solid State Commun.* **2008**, *148*, 538–540. [[CrossRef](#)]
22. Lim, C.S.; Wang, L.; Chua, C.K.; Sofer, Z.; Jankovský, O.; Pumera, M. High temperature superconducting materials as bi-functional catalysts for hydrogen evolution and oxygen reduction. *J. Mater. Chem. A* **2015**, *3*, 8346–8352. [[CrossRef](#)]
23. Goldschmidt, D.; Reisner, G.; Direktovitch, Y.; Knizhnik, A.; Gartstein, E.; Kimmel, G.; Eckstein, Y. Tetragonal superconducting family $(\text{Ca}_x\text{La}_{1-x})(\text{Ba}_{1.75-x}\text{La}_{0.25+x})\text{Cu}_3\text{O}_y$: The effect of cosubstitution on the transition temperature. *Phys. Rev. B* **1993**, *48*, 532. [[CrossRef](#)]
24. Mirmelshtein, A.; Podlesnyak, A.; Bobrovskii, V.; Davydov, S.; Karkin, A.; Kozhevnikov, V.; Goshchitskii, B.; Cheshnitskii, S. Electrical crystal field effects in high-temperature superconductor $\text{HoBa}_2\text{Cu}_3\text{O}_7$. *Phys. C Supercond.* **1988**, *153*, 176–177. [[CrossRef](#)]
25. Maple, M.; Dalichaouch, Y.; Ferreira, J.; Hake, R.; Lee, B.; Neumeier, J.; Torikachvili, M.; Yang, K.; Zhou, H.; Guertin, R. $\text{RBa}_2\text{Cu}_3\text{O}_{7-\delta}$ (R = Rare earth) High- T_c magnetic superconductors. In Proceedings of the Yamada Conference XVIII on Superconductivity in Highly Correlated Fermion Systems, Sendai, Japan, 31 August–3 September 1987; Elsevier: Amsterdam, The Netherlands, 1987; pp. 155–162.
26. Jankovský, O.; Sedmidubský, D.; Rubešová, K.; Sofer, Z.; Leitner, J.; Ružička, K.; Svoboda, P. Structure, non-stoichiometry and thermodynamic properties of $\text{Bi}_{1.85}\text{Sr}_2\text{Co}_{1.85}\text{O}_{7.7-\delta}$ ceramics. *Thermochim. Acta* **2014**, *582*, 40–45. [[CrossRef](#)]
27. Jankovský, O.; Sedmidubský, D.; Sofer, Z.; Šimek, P.; Hejtmánek, J. Thermodynamic behavior of $\text{Ca}_3\text{Co}_3.93\text{O}_{9+\delta}$ ceramics. *Ceram. Silik.* **2012**, *56*, 139–144.
28. Jankovský, O.; Sedmidubský, D.; Sofer, Z. Phase diagram of the pseudobinary system Bi-Co-O . *J. Eur. Ceram. Soc.* **2013**, *33*, 2699–2704. [[CrossRef](#)]
29. Kamihara, Y.; Hiramatsu, H.; Hirano, M.; Kawamura, R.; Yanagi, H.; Kamiya, T.; Hosono, H. Iron-based layered superconductor: LaOFeP . *J. Am. Chem. Soc.* **2006**, *128*, 10012–10013. [[CrossRef](#)]
30. Wu, M.-K.; Ashburn, J.R.; Torng, C.; Hor, P.H.; Meng, R.L.; Gao, L.; Huang, Z.J.; Wang, Y.; Chu, A. Superconductivity at 93 K in a new mixed-phase Y-Ba-Cu-O compound system at ambient pressure. *Phys. Rev. Lett.* **1987**, *58*, 908. [[CrossRef](#)]
31. Schneemeyer, L.; Waszczak, J.; Siegrist, T.; Van Dover, R.; Rupp, L.; Batlogg, B.; Cava, R.J.; Murphy, D. Superconductivity in $\text{YBa}_2\text{Cu}_3\text{O}_7$ single crystals. *Nature* **1987**, *328*, 601. [[CrossRef](#)]
32. Watkins, S.; Fronczek, F.; Wheelock, K.; Goodrich, R.; Hamilton, W.; Johnson, W. Structure of Y_2BaCuO_5 . *Acta Crystallogr. Sect. C* **1988**, *44*, 3–6.
33. Lee, D.; Selvamanickam, V.; Salama, K. Influences of Y_2BaCuO_5 particle size and content on the transport critical current density of $\text{YBa}_2\text{Cu}_3\text{O}_x$ superconductor. *Phys. C Supercond.* **1992**, *202*, 83–96. [[CrossRef](#)]
34. McGinn, P.; Chen, W.; Zhu, N.; Tan, L.; Varanasi, C.; Sengupta, S. Microstructure and critical current density of zone melt textured $\text{YBa}_2\text{Cu}_3\text{O}_{6+x}/\text{Y}_2\text{BaCuO}_5$ with BaSnO_3 additions. *Appl. Phys. Lett.* **1991**, *59*, 120–122. [[CrossRef](#)]
35. Jin, S.; Tiefel, T.; Kammlott, G. Effect of Y_2BaCuO_5 inclusions on flux pinning in $\text{YBa}_2\text{Cu}_3\text{O}_{7-\delta}$. *Appl. Phys. Lett.* **1991**, *59*, 540–542. [[CrossRef](#)]

36. Hlásek, T.; Shi, Y.; Durrell, J.H.; Dennis, A.R.; Namburi, D.K.; Plecháček, V.; Rubešová, K.; Cardwell, D.A.; Jankovský, O. Cost-effective isothermal top-seeded melt-growth of single-domain YBCO superconducting ceramics. *Solid State Sci.* **2019**, *88*, 74–80. [[CrossRef](#)]
37. Golosovsky, I.; Böni, P.; Fischer, P. Magnetic structure of Y_2BaCuO_5 . *Solid State Commun.* **1993**, *87*, 1035–1037. [[CrossRef](#)]
38. Štejfa, V.; Fulem, M.; Růžička, K.; Červinka, C. Thermodynamic study of selected monoterpenes III. *J. Chem. Thermodyn.* **2014**, *79*, 280–289. [[CrossRef](#)]
39. Kresse, G.; Furthmüller, J. Efficient iterative schemes for ab initio total-energy calculations using a plane-wave basis set. *Phys. Rev. B* **1996**, *54*, 11169. [[CrossRef](#)]
40. Perdew, J.P.; Burke, K.; Ernzerhof, M. Generalized gradient approximation made simple. *Phys. Rev. Lett.* **1996**, *77*, 3865. [[CrossRef](#)]
41. Dudarev, S.; Botton, G.; Savrasov, S.; Humphreys, C.; Sutton, A. Electron-energy-loss spectra and the structural stability of nickel oxide: An LSDA + U study. *Phys. Rev. B* **1998**, *57*, 1505. [[CrossRef](#)]
42. Forsyth, J.; Brown, P.; Wanklyn, B. Magnetism in cupric oxide. *J. Phys. C* **1988**, *21*, 2917. [[CrossRef](#)]
43. Martin, C. Simple treatment of anharmonic effects on the specific heat. *J. Phys. Condens. Matter* **1991**, *3*, 5967. [[CrossRef](#)]
44. Hengzhong, Z.; Zheng, F.; Pingmin, Z.; Xinmin, C. Enthalpies of formation of some phases present in the Y–Ba–Cu–O system by solution calorimetry. *J. Solut. Chem.* **1995**, *24*, 565–578. [[CrossRef](#)]
45. Zhou, Z.; Navrotsky, A. Thermochemistry of the Y_2O_3 –BaO–Cu–O system. *J. Mater. Res.* **1992**, *7*, 2920–2935. [[CrossRef](#)]



© 2019 by the authors. Licensee MDPI, Basel, Switzerland. This article is an open access article distributed under the terms and conditions of the Creative Commons Attribution (CC BY) license (<http://creativecommons.org/licenses/by/4.0/>).